

Effect of Set-Point Amplitude Variation of Kelvin Probe Force Microscope During Contact Charging of Muscovite Mica

Jose M. Esmeria, Jr.,^{1,*} and Romeric Pobre²

¹Central Instrumentation Facility, De La Salle University–Laguna Campus, Biñan City, Laguna, Philippines

²Department of Physics, De La Salle University, Manila, Philippines,

*Email: jose.esmeria@dlsu.edu.ph

ABSTRACT

We investigated the effect of varying the set-point amplitude of the Kelvin probe force microscope (KPFM) or an electric probe variant of the atomic force microscope for contact charging of muscovite mica at nanoscale resolution. We used the tapping mode of KPFM resonant at 300 kHz to observe noticeable surface potential on the muscovite mica by simply adjusting the amplitude set point A_{sp} at 40-, 30-, 20-, and 10-nm levels. Throughout the study, an *n*-type Si tip was used for KPFM with a nominal radius of 7 nm and +1 V direct current bias setting. With KPFM's scanning velocity set at 1.67 $\mu\text{m}/\text{sec}$ and lateral scanning frequency of 0.8 Hz, contact electrification was observed on a 21- μm -thick cleaved muscovite mica. At $A_{sp} = 40$ nm and 30 nm, results showed a consistent positive surface charge distribution that agrees well with the standard triboelectric series. However, at $A_{sp} = 20$ nm, the surface charge distribution suddenly changed into negative charge but eventually reverted when A_{sp} was set to 10 nm. The first sign reversal can be attributed to the electron field emission emanating from the *n*-type Si tip to the muscovite mica surface when the surface potential reached the -150-mV mark. On the other hand, the second sign reversal happened due to the back tunneling from the mica's surface to the tip.

Keywords: Muscovite mica, triboelectricity, AFM

INTRODUCTION

Muscovite mica is a material that is well-known in the electrical power industry as an excellent electrical insulator because of its

high dielectric constant and high-volume resistivity. Table 1 shows the common electrical and physical characteristics of muscovite mica in the market.

Table 1. Physical and Electrical Properties of Muscovite Mica

Chemical formula	$\text{KAl}_2(\text{AlSi}_3\text{O}_{10})(\text{F},\text{OH})_2$ ^a
Physical properties	Cleavage: {001} perfect; partings on {110}, {010}.
Color	White to colorless, silvery white, and tinged various colors by impurities ^a
Density	2.77–2.88 g/cm ^{3b}
Hardness	2½ on Mohs scale ^b
Dielectric strength: @20 °C	3–5 kV/mm ^b
Volume resistivity	10 ¹³ to 10 ¹⁷ Ω-cm ^b
Crystal data	Monoclinic. Point group: 2m: Crystals tabular to columnar k [001] ^c
Unit cell	a = 5.199 Å, b = 9.027 Å, c = 20.106 Å, β = 95.78° ^d

^aKalita & Wary (2016, p. 53).

^b“Properties and Chemical Composition of Mica Grade V1” (2021).

^c“Muscovite” (2021).

^dDe Poel et al. (2014, p. 19).

Muscovite mica sheets are typically used as a radiation detector window, plastic component material, dielectric material for capacitors, asphalt-roofing component material, and many other materials applications. One outstanding physical feature of this material is its atomically flat surface under nominal conditions. With this unique feature, mica has earned so much research interest in the field of thin films, high-resolution surface metrology, and organic electronics (Zhang et al., 2016, p. 3755), to name a few. A typical 10 × 13-cm²-sized freshly cleaved mica specimen has a single terminated surface without any surface protrusion and steps no higher than 35 nm (De Poel et al., 2014, p. 23). Its atomically flat surface property has been the semiconductor industry standard for surface metrology calibration when using an atomic force microscope (AFM). Moreover,

mica’s freshly cleaved surface makes an ideal substrate for 6P organic electronics (Frank et al., 2007, pp. 2152–2160). Aside from its flatness, mica’s high electrostatic charge yield gained much interest in developing the next-generation energy-harvesting devices. One of its interesting applications is electrets for field effect transistors or FET (Zhang et al., 2016, p. 3755) and triboelectric nanogenerators or TENGs. TENGs are self-powering devices that harness electrostatic surface charge generated during contact electrification (CE; Wang et al., 2020, pp. 2–5). These devices take advantage of the kinetic energy being drawn from the physical movement of the human body being converted into electrostatic potential energy by CE (Wang et al., 2019, p. 2). Muscovite mica belongs to the group of naturally occurring clay minerals, with the chemical

formula $\text{KAl}_2(\text{Si}_3\text{Al})\text{O}_{10}(\text{OH})_2$ - (Christenson & Thomson, 2016, pp. 367–390). The muscovite structure is a dioctahedral, in which a charged layer arises from 1 in 4 atomic layered substitutions of Al^{3+} ions with Si^{4+} ions in the tetrahedral layer and the 2:1 layer being held together by K^+ . The negatively charged aluminosilicate layers

AlO_6 that arises from a substitution of a quarter of the Si^{4+} ions by Al^{3+} ions. Figure 1 shows the crystal structure of muscovite mica along the $\{001\}$ plane or *c-axis*. These layers are a perfect location to cleave mica at the $\{001\}$ plane where K^+ cations are being held by weak electrostatic force.

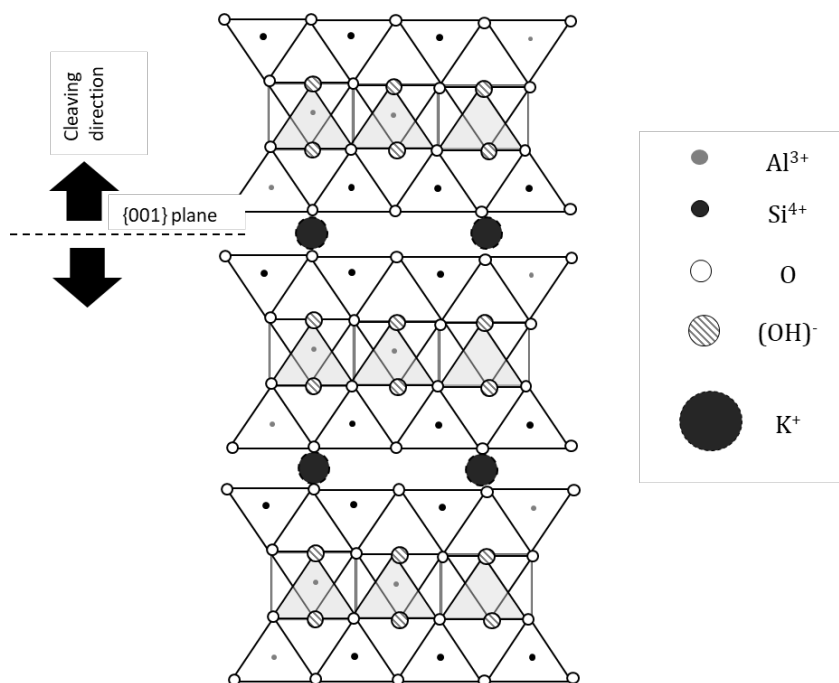


Figure 1. Structure of muscovite mica with two tetrahedral layers of SiO_4 above and below an octahedral layer of AlO_6 , where the layers are held by the weak electrostatic force mediated by the K^+ ions. The arrows show the perpendicular direction along the $\{001\}$ basal plane of the mica crystal, wherein perfect cleaving can be applied.

Cleaving of a mica sheet along the basal plane results into half of K^+ ions present in a single layer of the crystal while the other half of the K^+ ions remained attached to the other face. This even distribution of K^+ cations leads to a positive charge on the surface of the mica (Christenson & Thomson, 2016, p. 8). The perfect cleaving results into a uniform flat surface with very minimal protrusion, which makes it ideal for surface studies that

require extremely uniform landscape with insignificant protrusions, aside from its excellent dielectric qualities. Limited studies were done so far in the electrostatic characterization of muscovite mica, and most of these studies were mostly focused on its macroscopic or bulk properties. In this paper, the authors will attempt to induce CE on muscovite mica by using the tapping mode of an *n*-type Si tipped Kelvin probe force

microscope (KPFM). This study will aid scientists and technologists to have mesoscopic understanding of mica material as an alternative source of electrostatic potential energy arising from triboelectrification or surface CE.

THEORY

CE

CE is a well-known physical phenomenon in electrostatics in which, when two materials come into contact, electric charge surfaces on materials after separation. However, this phenomenon is poorly understood when it is scaled down and

analyzed in the mesoscopic scale. Thus, there is a need for a deeper understanding of the surface physics where different charging mechanisms like ionic exchange, charge affinity, and contact force can be ascertained in this kind of study. To rank different materials according to their charge affinity characteristics from the most positive (deficient in electrons) to the most negative (excess in electrons), Zou et al. (2020) listed down the triboelectric series as shown in Figure 2 below. Mica has demonstrated the highest positive affinity compared to common materials like silicone rubber and polydimethylsiloxane (PDMS; Zou et al., 2019, p. 6).

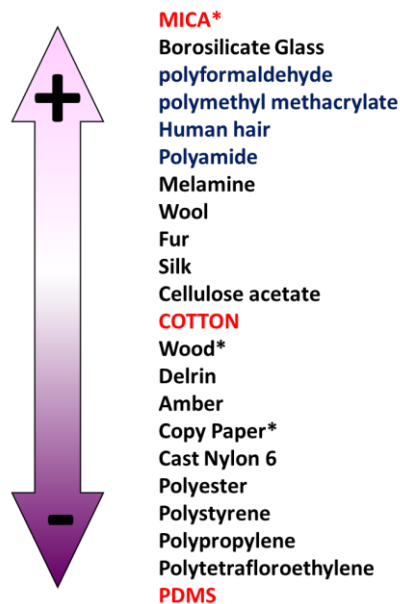


Figure 2. Triboelectric series of common materials from mica, which carries the most positive charge affinity material down to polydimethylsiloxane (PDMS), which has the most negative affinity material.

The process of CE differs on the nature of bi-materials in contact (metal-insulator,

insulator-insulator) when various charging mechanisms are at play (Lacks & Mohan

Sankaran, 2011, p. 1). Dielectric materials usually generate bipolar charging surfaces due to ionic and materials transfer after frictional contact (Williams, 2012, p. 6). This ionic exchange and moieties charge transport happens during repeated contact and separation between two materials (Zhang et al., 2020, p. 11676). The repeated action gives rise to the stochastic behavior of the charging process on dielectrics where there is a random interplay between ionic exchange and moieties charge transport on the bulk surfaces of the material. This random nature of charge production between ionic exchange or moieties transfer explains the difficulty of repeatable measurements due to its high variability in the macroscopic regime of triboelectric studies (Baytekin et al., 2012, p. 4924). To add complexity in the CE, impact force or frictional rubbing would also lead to material transfer, which is responsible for the polarization of the surface material (Wang & Wang, 2019). A recent study has shown that the electron transfer is the dominant mechanism that can be attributed to triboelectricity or CE. Electron transfer can be best ascertained by the solid-solid, liquid-solid, and liquid-liquid interface material separation and consequently charge generation. Electron transfer also occurs when interatomic distance between two materials is less than or comparable to the ionic bond length of 0.2 nm (Wang & Wang, 2019, p. 35).

Kelvin Probe Force Microscopy: A Variant of AFM

An electric field probe device can be used for a rapid macroscopic surface potential characterization after CE (Noras, 2003, p.

13). However, data integrity can be compromised with this kind of probe due to the instrument's dependence on the probe to surface displacement. The utilization and application of AFM addressed this measurement limitation even at the submicron resolution. AFM with a function of KPFM is used to scan the surface potential of materials with very high resolution at a submicroscopic scale. The KPFM probe, which is an optional function of a commercial type of AFM, is an excellent tool for imaging a surface potential map by measuring its work function via contact potential difference. This particular AFM method can be modelled like a capacitor between the tip of the probe and the sample surface (Melitz et al., 2011). This special function of AFM enables the wielder to generate both topographical and electric potential image maps simultaneously. To understand the different forces acting on the tip of AFM, the following section describes the physics behind AFM. The cantilever tip function is related to the energy of the capacitance C between the tip and the sample as shown in Equation 1. The electrostatic force $F_{ef}(z)$ between the tip and sample surface is then related to the differential of capacitance C as a function of the vertical height z :

$$F_{ef}(z) = -\frac{1}{2} \frac{dC(z)}{dz} (\Delta V)^2 \quad (1)$$

where ΔV is the voltage displacement between the tip and surface and $dC(z)/dz$ is the capacitance gradient dependent on the vertical distance z between sample and tip. The potential difference ΔV is expressed as

$$\Delta V = V_{ac} \sin \omega t + V_{dc} \pm V_{cpd} \quad (2)$$

The \pm symbol in Equation 2 is the applied bias convention, and for this study, direct current (DC) bias was applied on the AFM's probe tip, so the $(-)$ sign convention is used in the following derivations. $V_{ac}\sin\omega t$ is the AFM oscillating drive of the AC voltage, and ω is the cantilever resonant frequency.

Substituting Equation 2 to Equation 1 and expanding Equation 1, the resulting equation yields

$$F_{ef}(z) = -\frac{1}{2}[(V_{cpd} - V_{dc}) + V_{ac}\sin\omega t]^2 \frac{\partial C(z)}{\partial z} \quad (3)$$

From Equation 3, three components can be derived by expanding it further into the following:

$$F_{DC} = -\frac{1}{4} \frac{\partial C(z)}{\partial z} [(V_{cpd} - V_{dc})^2] \quad (4)$$

$$F_{\omega} = -(V_{cpd} - V_{dc}) \frac{\partial C(z)}{\partial z} V_{ac}\sin\omega t \quad (5)$$

$$F_{2\omega} = -\frac{1}{4} \frac{\partial C(z)}{\partial z} V_{ac}^2 (1 - \cos 2\omega t) \quad (6)$$

Equation 4 is the force experienced by the tip surface during potential imaging, while Equation 5 is an amplitude modulated force exerted on the AFM tip due to the electric field generated when the AFM tip and material slightly separates. The force component in Equation 6 is considered for capacitance microscopy (Melitz et al., 2011) and has no effect on the mechanical oscillation since Equation 6 relates only to the square of the alternating current (AC) driving voltage V_{ac} and the capacitance gradient $\frac{\partial C(z)}{\partial z}$. When the sample and AFM tip is in quasi-contact, the Fermi level is maintained, and it would result into a contact potential difference V_{cpd} . However, this

creates an electrostatic force F_{ω} exerted on the AFM tip due to the electric field generated between the two materials. In Equation 5, F_{ω} is amplitude modulated by $V_{ac}\sin\omega t$, where it distorts the mechanical oscillation of the tip $F_{ef}(z)$ due to the enveloping effect that affects the signal during surface scanning. By applying an opposite DC bias voltage V_{DC} , it eliminates the enveloping effect of F_{ω} that left two force components F_{DC} and $F_{2\omega}$ unabated, which is the net electrostatic force that envelopes the signal.

CE Using AFM Tip

AFM scanning involves two widely used imaging modes: contact and tapping mode. Contact mode uses a constant force application on the tip, which is in constant contact with the surface. Contact mode was a well-known method to generate CE, since it provides true contact and applied force on the tip that can be controlled. However, constant contact with the surface may cause signal artifacts and lateral friction, thereby damaging the soft surfaces under study. Meanwhile, the tapping mode of AFM provides a gentler approach in scanning without damaging the surface of the samples besides getting a higher image resolution. In this mode, a driving sinusoidal voltage vibrates the AFM probe at a few hundred kilohertz frequencies. In so doing, the tip taps with the surface of the sample at high contact-separation repetition rates. Increasing the scanning speed and oscillating frequency will ensure a quasi-continuous contact to the surface (Zhou et al., 2016, p. 3706–3707). The tip oscillation is controlled by the input AC drive voltage (with feedback), to keep constant amplitude along

the surface. Increasing the AC drive voltage increases the sinusoidal amplitude that consequently increases the contact force of the tip. Figure 3 illustrates how tapping and the cantilever are being driven by an AC signal along with a DC bias voltage applied to the tip. The dynamic motion of the tapping mode can be expressed as a single degree of freedom (Equation 7) damped harmonic oscillator (Legleiter, 2009, pp. 3–4):

$$m_{eff} \frac{d^2z}{dt^2} + b \frac{dz}{dt} + k\{A_{sp} - z_o + a_o \sin \omega t\} = F_{tip} \quad (7)$$

where F_{tip} is the tip to sample force, A_{sp} is the cantilever tip position with respect from the surface (or amplitude set point, A_{sp}), ω is the drive frequency, z_o is the cantilever reference position, b is the damping coefficient, k is the cantilever spring constant, and m_{eff} is the effective mass of the cantilever. Since tapping mode is a continual change in separation between the tip and sample surface, one of the solutions from Equation 7 is when the separation (z_c) between the tip and the surface is large, then the force imparted on the tip will be as follows (Legleiter, 2009, p. 3):

$$F_{tip} = \frac{HR_{tip}}{6z_c^2} \quad \text{for } z_c > a_o \quad (\text{long range attractive region}) \quad (8)$$

The force on the tip can be considered as Van der Waals force acting on a sphere. In Equation 8, H is Hamaker's constant, which is $\sim 12.8 \times 10^{-20}$ J for mica in air (Bergström, 1997, p. 152); a_o is the interatomic distance of the sample material; and R_{tip} is the AFM tip radius. When the tip is in contact with the surface, such that $z_c < a_o$, the force in this case is repulsive, and it can be expressed in Equation 9 as

$$F_{tip} = \frac{4}{3\pi k_{eff}} \sqrt{R} (a_o - z)^{\frac{3}{2}} - \frac{HR_{tip}}{6a_o^2} \quad \text{for } z_c < a_o \quad (\text{short range repulsive region}) \quad (9)$$

The effective spring constant k_{eff} is then

$$k_{eff} = \frac{1-\nu_{tip}^2}{\pi Y_{tip}} + \frac{1-\nu_{sample}^2}{\pi Y_{sample}} \quad (10)$$

where ν_{tip}^2 and ν_{sample}^2 are Poisson's coefficient, while Y_{tip} and Y_{sample} are Young's modulus of the tip and sample, respectively. Tapping mode scanning of AFM is mainly characterized by A_{sp} . A_{sp} is the oscillation amplitude of the tip with respect to the surface shown (Figure 3). The set point refers to the location of the tip at the crest of amplitude with respect to the surface.

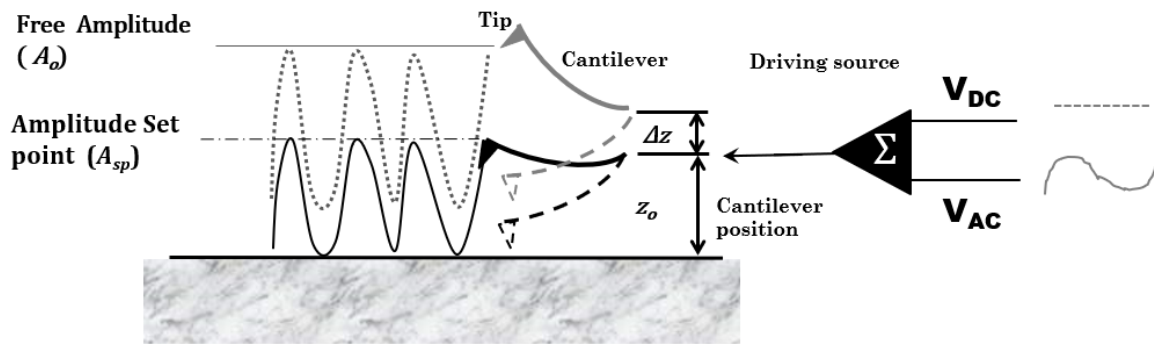


Figure 3. Illustration of tapping mode, showing the free amplitude A_o is the full cantilever swing brought about by the AC drive voltage V_{ac} . Amplitude set point or A_{sp} is the tip-to-surface swing of the cantilever. Increasing A_{sp} , by increasing the cantilever position z_o , increases the tip-to-surface distance. Lowering the A_{sp} will increase the tapping force exerted on the sample.

When the cantilever position is lifted at a height Δz , the tip no longer in contact with the surface, then and only then does the cantilever swing freely, and it can be characterized by free amplitude A_o . The contact tip force of the AFM is dependent on A_{sp} and cantilever position. Lowering the value of A_{sp} increases the force imparted on the tip, and the deflection force increases as described in Equation 8.

MATERIALS AND METHOD

A noncontact electrostatic voltmeter (TREK 520) was used to check the CE created after frictional force application of PDMS and a cotton swab. Figure 2 clearly shows that PDMS has the most negative charge affinity and cotton swab is considered neutral but with a slight charge affinity at the positive end. In this experiment, the electrostatic probe was placed 5 mm above the surface of the mica specimen, while a frictional contact was applied in one direction for five times on the surface using PDMS and then the cotton swab. The AFM equipment used in the study

is a Bruker model *Dimension ICON* AFM with KPFM function. The AFM model housed in an acoustic and electromagnetic interference enclosure shields the scanner from environmental noise but operates at atmospheric pressure. The AFM tip (*Bruker model OTESPA R3*) is an *n*-type Si- heavily doped with Sb ($N_D \approx 6 \times 10^{18}/\text{cm}^3$), which corresponds to a volume resistivity of 0.01~0.02 $\Omega\text{-cm}$ operating at $E_f = 1.07$ eV Fermi level. The cantilever has a spring constant of 26 N/m, and the backside is coated with Al film of 100-nm thickness. The AFM tips have a nominal radius of about 7 nm tapping at ~ 300 kHz resonant frequency. The tip velocity is set at $\sim 1.67 \mu\text{m/s}$, the lateral displacement of which during scanning is approximately $\sim 0.6 \text{ \AA}$ between each tap on the surface. These extremely small lateral movements simulate a continuous scanning without damaging the surface. Potential map images shown here are represented by three color palettes: *blue* color represents the positive potential, *red* color represents the negative potential, and *yellow-green* color represents neutral or zero potential surface.

To optimize the AFM’s tip tapping oscillation, the auto-tuning function of the AFM was enabled prior to the scanning of any images; this procedure ensures that the tip oscillates at its resonant frequency. The *Ramp* software function of the Bruker AFM was used to estimate the force applied on the tip with reference to its position from the surface (Kelley, 2010, pp. 221–224). This function lowers the cantilever position z_o in Figure 4 until the tip hits the surface and the amplitude reaches the minimum. In Figure 5,

$z_o = 0$ was used as the reference start point, and the *Ramp* function adjusted the cantilever height until it reached $z_o = 700$ nm, wherein the tip hits the surface. At this point, the amplitude (tip swing) was abruptly reduced by 50%, and the force on the tip reached its maximum. The Ramp function calculates (Kelley, 2010, p. 305) both the force imparted on the tip and the tip deflection. Using the data obtained in Figure 5, the force on the tip or F_{tip} , A_{sp} , and tip deflection were plotted, and they show a linear relationship.

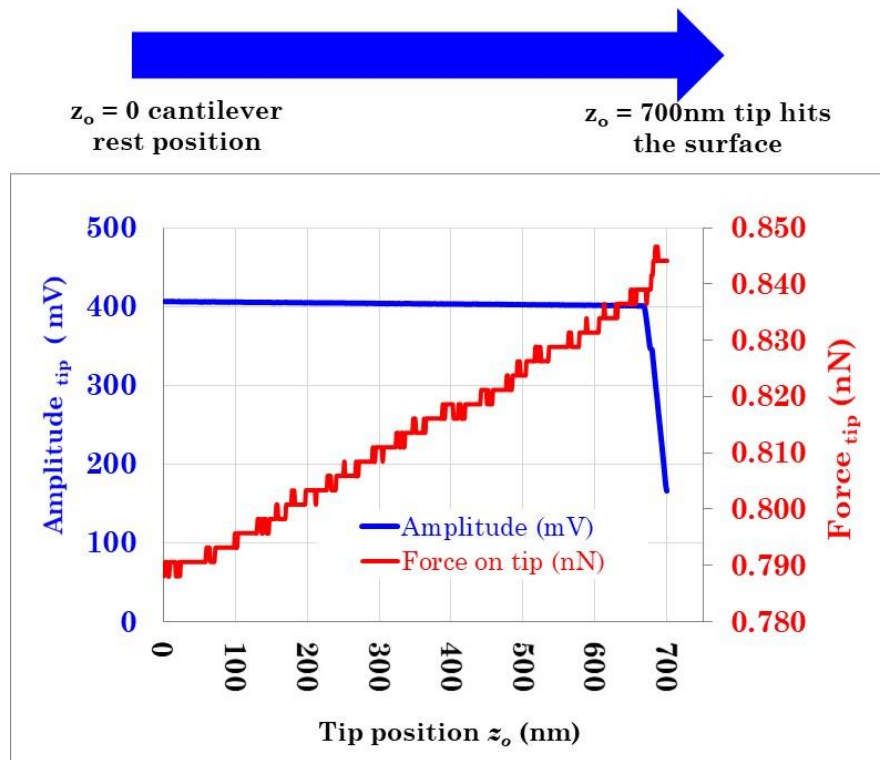


Figure 4. The Ramp function is used to calculate the force applied on the tip as well as its deflection; the cantilever position z_o is adjusted from zero (rest position) until it reaches a maximum of 700 nm.

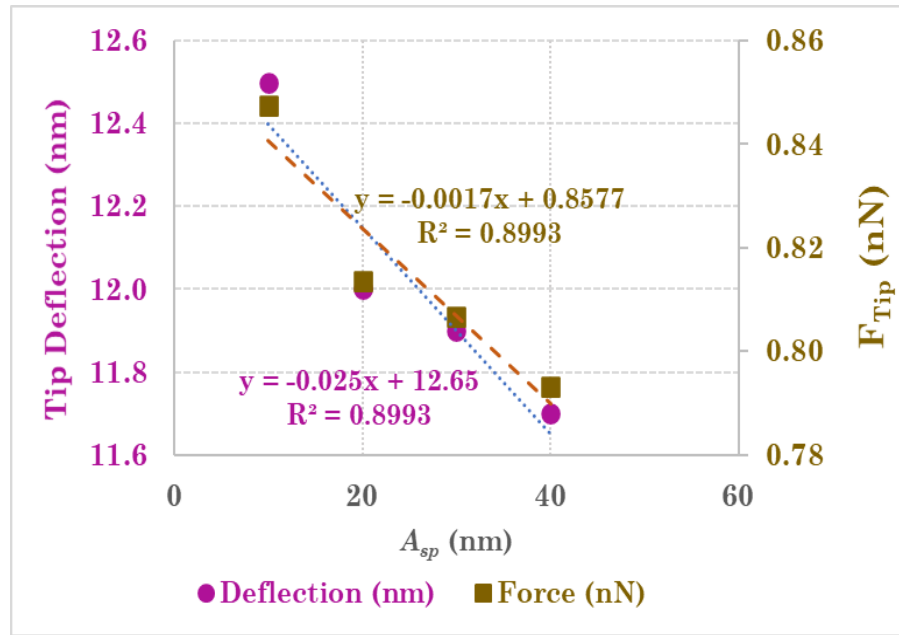


Figure 5. Linear relationship of AFM tip deflection and force imparted on tip as the amplitude set point is varied.

The muscovite mica sample used in this study is a high-grade *V-1* material from SPI Supplies (“Muscovite Mica Substrates,” 2021). The sample is grayish transparent material with dimensions of 12 mm in diameter and 0.15 mm in thickness and volume resistivity of $\sim 10^{15-17} \Omega\text{-cm}$. After the mica was cleaved, the sample’s surface was gently wiped in one direction with a cotton swab dipped into propanol. A stainless plate (50 mm \times 40 mm \times 1 mm) was used as a mounting fixture where the sample was secured by a conductive carbon tape with $10^6 \Omega\text{-cm}$ resistivity. The DC bias applied on the AFM tip was fixed at $V_{dc} = +1$ Volt and set at a scan size of $1 \mu\text{m} \times 1 \mu\text{m}$ with an aspect ratio of 1:1. Resolution was set to 256 sampling/line at 128 lines. The scanning frequency was fixed at 0.8 Hz to minimize background noise during scanning. The experiments were carried out in a manufacturing environment, where relative humidity was fixed at $55 \pm 5\%$, since this was

the default setting in the laboratory. Also, the humidity affects the outcome of CE due to the presence of water layer on the surface that could rapidly neutralize the electric charges on the surface. A fixed relative humidity on the surface would eliminate charge variability on the surface charge during measurement. In vacuum conditions, the electric charge could remain for a longer period due to absence of neutralizing ions. However, experiments to verify using vacuum conditions cannot be performed due to the absence of ultra-high vacuum AFM. CE is not affected by temperature and ambient pressure change. The room temperature was maintained at $20 \pm 5 \text{ }^\circ\text{C}$ and is also the default environmental setting of the lab. The environmental conditions reflect the real-world applications for triboelectric energy research.

RESULTS AND DISCUSSION

Table 2 shows the macroscopic measurement of cleaved mica, contact electrified by PDMS and a cotton swab. The parallel line in between the two materials denotes frictional contact between the two materials. The first two columns on the left show that mica, after being frictionally rubbed with PDMS, generates a positive charge with an average surface potential of +21.2 V, whereas the PDMS material has a negative affinity with an average surface potential of -1278 V (Esmeria et al., 2019, p. 2E-02-2, 2-3). The two columns on the right show the same mica generates a positive charge when frictionally rubbed with a cotton swab. These results verified that mica has a

positive affinity in the triboelectric series, irrespective of the sign affinity of the material it contacts. Mica being a good dielectric has a positive charge in the triboelectric series because it has lower work function than other common materials. Based on a recent study, the mica work function is estimated to be 1.8 eV (Zou et al., 2020, p. 6), in comparison with *n* doped Si of 4.6 eV. Freshly cleaved mica contains uniformly distributed K⁺ ions on both surfaces, which ideally would make it neutral. However, half of these K⁺ ions are attracted to the substitutional sites in Al and O, thus creating a dipole (Müller & Chang, 1968, pp. 455–458).

Table 2. Macroscopic Measurement Using Noncontact Electrostatic Potential Meter

	PDMS // Mica	Cotton // Mica
Average	-1,278.8 +21.2	+2.8 +14.2
Maximum	-1,400.0 +24.0	+5.0 +22.0
Minimum	-1,200.0 +18.0	+2.0 +10.0

Note. The parallel line denotes the two materials are in CE.

The potential map images after CE in tapping mode are shown in Figure 6. Initially at $A_{sp} = 40$ nm, the surface displayed a deep blue color contrast indicative of holes majority carrier on the surface, which agrees with the positive sign outcome measured from the electrostatic voltmeter. Red spikes visible from the side view images represent

trapped electrons. Mica has trap states that are occupied by electrons when equilibrium is reached (Hashimoto & Sakakibara, 2000, pp. 231–235). A similar situation was also observed at set point 30 nm but with fewer negative charges. In Figure 6b to 6c, charge sign reversed after the set point was lowered from 30 to 20 nm.

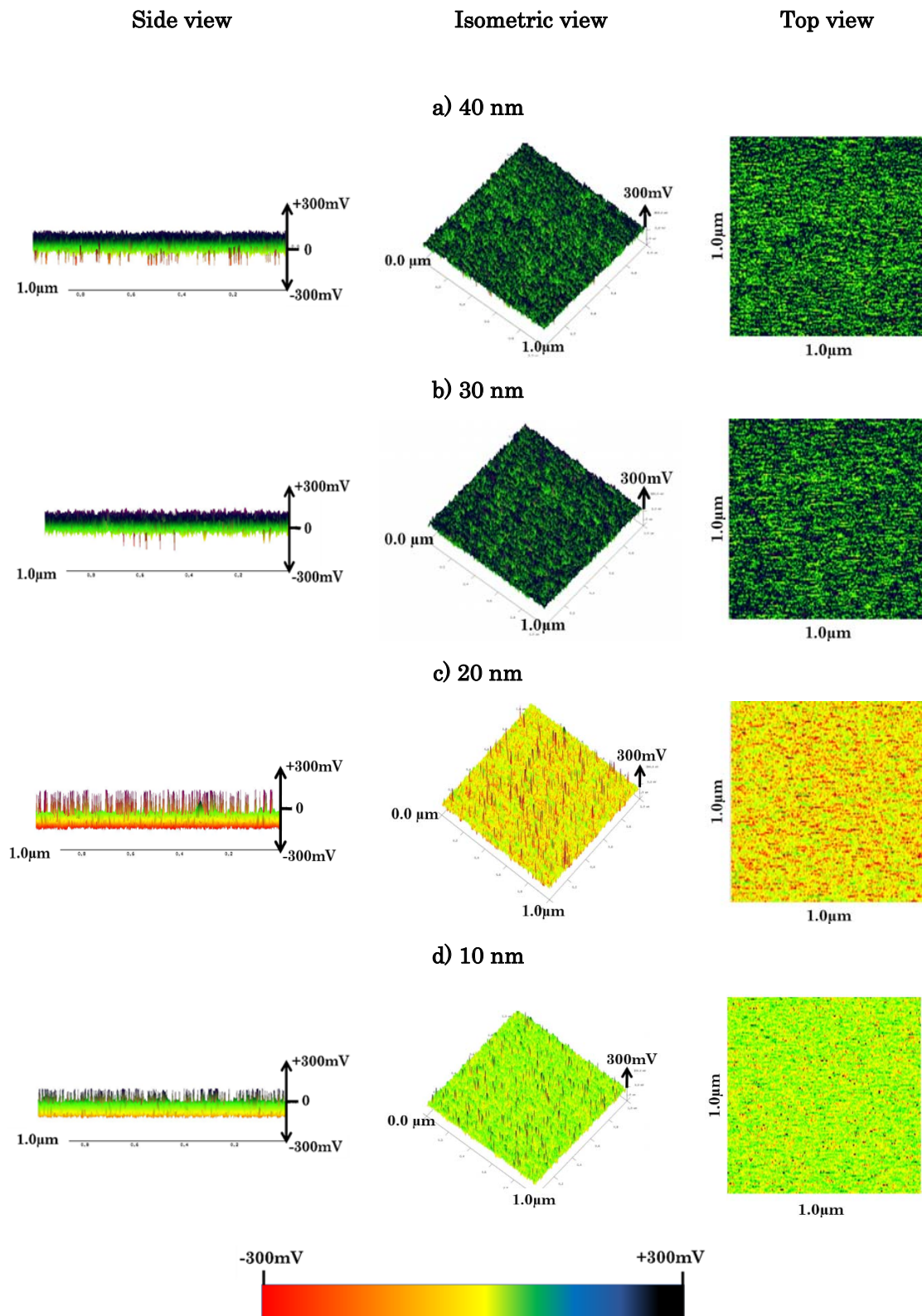


Figure 6. Surface potential images at different amplitude set point A_{sp} , with sequence from 40 to 10 nm. The top view and isometric view show the spikes at the surface, which indicate positive values (side view) from **a** to **b**. Sign reversal occurs in **c**, and the surface potential flipped back to positive in **d**.

In Figure 6d, the surface charge is partly neutralized with blue points, which indicates minor positive charge affinity.

Mica Contact-Charging Mechanism

Mica contact charging at nanoscale can be attributed to electron transfer through back tunneling. The proximity of the DC biased AFM tip to the mica surface causes electron field emission towards the mica surface. The repeated tapping of the tip could give rise to an electron cloud overlap (or back tunneling) depending on the tip force and strain on the surface (Pan & Zhang, 2018, p. 6). It can also be surmised that electron transfer occurs (Wang & Wang, 2019, pp. 39–41) when the potential barrier of the material is overcome by the electrons. Contact charging by electron cloud overlap is the dominant charging mechanism when it comes to dielectric materials that have different Fermi levels. Moreover, the silicon tip and mica are similar to a semiconductor/insulator interface, wherein electron transfer largely depends on the Fermi and quasi-Fermi levels of silicon and mica, respectively. A positive DC bias applied to *n*-type silicon causes charge

reversal when there are more holes on its surface due to electron vacancies that resulted into positive charge. These surfaces with positive potential map images are more evident in Figure 6a and 6b. However, a complete potential surface sign reversal occurred in Figure 6c when A_{sp} was set to 20 nm. Lowering A_{sp} reduces the tip-to-surface gap and increases the force imparted on the tip (Figure 5). The electron charge builds up on the surface, and the small gap between the AFM tip and mica surface (~ 0.5 nm to 1 nm) has caused the electrons to be discharged on the mica surface. The partial neutralization in Figure 6d can be attributed to the back tunneling from the mica surface to the Si tip. At the instance of contact with the mica surface, electrons were discharged to the mica surface. During this instance, the electric fields had arisen between the gap due to the excess electrostatic charges on the surface of the mica. This gives rise to surface energy states of the mica with respect to the *n*-type Si tip. On the other hand, back tunneling to the *n*-type Si tip can happen during separation when there are sufficient empty surface states on the tip. The diagram in Figure 7a to 7c demonstrates the process of charge transfer and back tunneling.

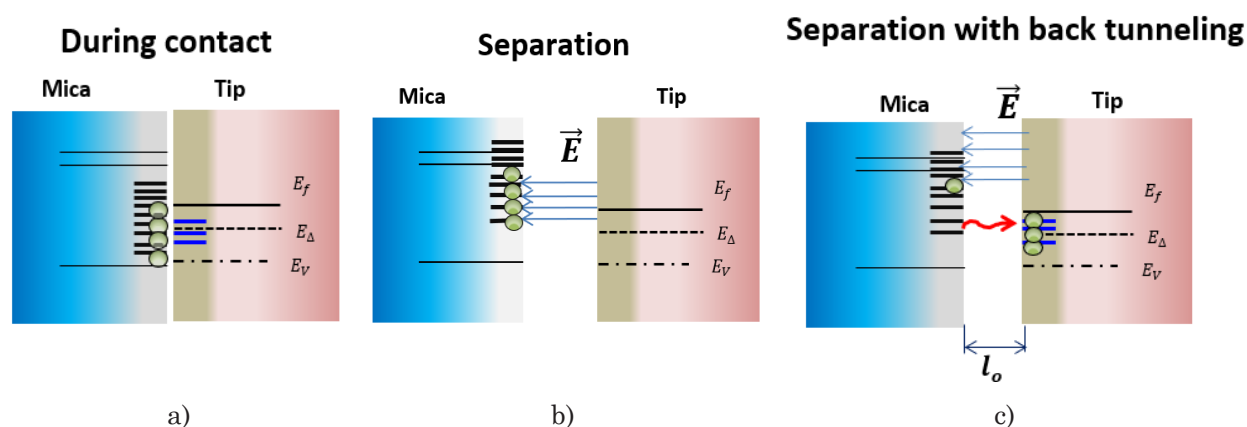


Figure 7. a) During contact, there are empty states in the mica that are higher compared to the Fermi level of silicon. b) Upon separation, the electric field created between the two surfaces increases the energy of the states in the mica, way above the Fermi level of Silicon. c) If there are sufficient lower density empty states in the silicon, the electrons can back tunnel to the tip, thus creating a more positive charge for the mica (Figure 6d).

An approximation of the back tunneling gap length l_o (Lowell, 1979, pp. 1541–1553) is as follows:

$$l_o = \frac{\epsilon_o E_\Delta}{N_o e^2} \quad (11)$$

This approximation shows that back tunneling can occur if the discrete surface state energy E_Δ of mica is equal to or higher than the Fermi level of the silicon tip. Using Equation 11, $\epsilon_o = 8.86 \times 10^{-12}$ C/V·m, the electron charge $e = 1.062 \times 10^{-19}$ C, and $E_\Delta = 3.58$ eV and N_o is 3.7×10^{17} /eV·m². Mica is a dielectric with no fixed Fermi level, only the quasi-Fermi band that exists at 5.0 eV and with a band gap of 4.2 eV (Hashimoto & Sakakibara, 2000, pp. 231–235) above valence band. Using these values in Equation 11, the calculated gap for back tunneling is $l_o \approx 0.5$ nm, which is approximately the intermolecular distance of mica. Trapped surface states exist also along with energies of 2.78 eV from the valence band (Kalita & Wary, 2016, p. 56). These surface states, when filled, are way above the Fermi level of this *n*-type Si ($E_f = 1.07$ eV) and may tunnel back to the tip.

CONCLUSION

Nanoscale CE of mica was demonstrated by using the AFM-KPFM tapping mode. Due to mica's lower work function compared to other materials, mica is generally a positive charging material commonly positioned at the top of the triboelectric series. Mica's positive charge affinity was verified both macroscopically using a noncontact electric field meter and nanoscopically using the AFM-KPFM method. The influence of set-point amplitude, which varies the force on the tip, has shown sign reversal when the set

point approaches the interatomic distance of the surface. The sign reversal can be attributed more to the electron field emission than to the back tunneling. Electron field emission from the tip to the surface occurs when the tip achieves enough charges to discharge it back to the mica surface when electron vacancies are enough, while back tunneling incidence happens when an electric field raises the energy of the states of mica after surface separation. In this case, the electrons tend to move from the occupied surface states and eventually tunnel through the *n*-type Si tip potential barrier and consequently occupy vacant lower energy surface states. The calculated back tunneling length during separation based on the physical parameters of the experimental setup is approximately 0.5 nm.

ACKNOWLEDGEMENT

The corresponding author would like to give his sincerest appreciation to his former colleagues in TDK Philippines Corp. (TPC); Ms. Melissa Gatan, for her assistance during AFM/ SPM set up and to Mr. Arun Khanna, for allowing the corresponding author some AFM time at TPC Reliability Engineering Laboratory during his employment in TPC.

REFERENCES

- Baytekin, H. T., Baytekin, B., Incorvati, J. T., & Grzybowski, B. A. (2012). Material transfer and polarity reversal in contact charging. *Angewandte Chemie*, 124(20), 4927–4931. <https://doi.org/10.1002/ange.201200057>
- Bergström, L. (1997). Hamaker constants of inorganic materials. *Advances in Colloid and Interface Science*, 70, 152.

- [https://doi.org/10.1016/s0001-8686\(97\)00003-1](https://doi.org/10.1016/s0001-8686(97)00003-1)
- Christenson, H. K., & Thomson, N. H. (2016). The nature of the air-cleaved mica surface. *Surface Science Reports*, *71*(2), 367–390.
- De Poel, W., Pinteá, S., Drnec, J., Carla, F., Felici, R., Mulder, P., Vlieg, E. (2014). Muscovite mica: Flatter than a pancake. *Surface Science*, *619*, 19–24.
- Diaz, A. F., & Felix-Navarro, R. M. (2004). A semi-quantitative tribo-electric series for polymeric materials: The influence of chemical structure and properties. *Journal of Electrostatics*, *62*, 277–290.
- Esmeria, J. M., Lacuesta, T., & Pobre R. (2019). 2019: *Proceedings of the 37th Samahang Pisika ng Pilipinas Physics Conference*. <https://proceedings.spponline.org/issue/view/SPP-2019>
- Frank, P., Hlawacek, G., Lengyel, O., Satka, A., Teichert, C., Resel, R., & Winkler, A. (2007). Influence of surface temperature and surface modifications on the initial layer growth of para-hexaphenyl on mica (001). *Surface Science*, *601*(10), 2152–2160.
- Hashimoto, Y., & Sakakibara, T. (2000). Surface states of mica and contact charging. *Japanese Journal of Applied Physics*, *39*(Part 1, No. 1), 231–235. <https://doi.org/10.1143/jjap.39.231>
- Kalita, J., & Wary, G. (2016). Estimation of band gap of muscovite mineral using thermo-luminescence (TL) analysis. *Physica B: Condensed Matter*, *485*, 53–59.
- Kelley, V. (2010). *Dimension Icon with Scan Assist instruction manual 004-1023-000 (Rev E)*. Bruker Nano Surfaces.
- Lacks, D. J., & Mohan Sankaran, R. (2011). Contact electrification of insulating materials. *Journal of Physics D: Applied Physics*, *44*(45), 453001. <https://doi.org/10.1088/0022-3727/44/45/453001>
- Legleiter, J. (2009). The effect of drive frequency and set point amplitude on tapping forces in atomic force microscopy: Simulation and experiment. *Nanotechnology*, *20*(24), 245703.
- Lowell, J. (1979). Tunnelling between metals and insulators and its role in contact electrification. *Journal of Physics D: Applied Physics*, *12*(9), 1541–1554. <https://doi.org/10.1088/0022-3727/12/9/016>
- Melitz, W., Shen, J., Kummel, A. C., & Lee, S. (2011). Kelvin probe force microscopy and its application. *Surface Science Reports*, *66*(1), 1–27.
- Müller, K., & Chang, C. (1968). Low energy electron diffraction observations of electric dipoles on mica surfaces. *Surface Science*, *9*(3), 455–458. [https://doi.org/10.1016/0039-6028\(68\)90149-0](https://doi.org/10.1016/0039-6028(68)90149-0)
- Muscovite. (2021). <https://geology.com/minerals/muscovite.shtml>
- Muscovite mica substrates. (2021). *SPI Supplies*. <https://www.2spi.com/category/mica-substrates/substrates/>
- Noras, M. (2003). Charge detection method of dielectrics—Overview. *Trek Application Note*, (3005), 1–13. <https://www.advancedenergy.com/globalasset/s/resources-root/application-notes/en-esvm-charge-detection-methods-application-note.pdf>
- Pan, S., & Zhang, Z. (2018). Fundamental theories and basic principles of triboelectric effect: A review. *Friction*, *7*(1), 2–17. <https://doi.org/10.1007/s40544-018-0217-7>
- Park, J. Y., & Salmeron, M. (2013). Fundamental aspects of energy dissipation in friction. *Chemical Reviews*, *114*(1), 677–711. <https://doi.org/10.1021/cr200431y>
- Properties and chemical composition of mica grade V1. (2021). https://www.tedpella.com/vacuum_html/Mica_Grade_V1_Properties.htm 9(9), 1304 (1–11). https://doi.org/10.3390/nano9_091304
- Wang, J., Qian, S., Yu, J., Zhang, Q., Yuan, Z., Sang, S., Sun, L. (2019). Flexible and wearable PDMS-based triboelectric nanogenerator for self-powered tactile sensing. *Nanomaterials*, *9*(9), 1304 (1–11). <https://doi.org/10.3390/nano9091304>
- Wang, J., Zhou, L., Zhang, C., & Lin Wang, Z. (2020). *Small-scale energy harvesting from environment by triboelectric nanogenerators. A guide to small-scale energy harvesting techniques*. <https://doi.org/10.5772/intechopen.83703>
- Wang, Z. L., & Wang, A. C. (2019). On the origin of contact-electrification. *Materials Today*, *30*, 34–51. <https://doi.org/10.1016/j.mattod.2019.05.016>
- Williams, M. W. (2012). Triboelectric charging of insulating polymers—some new perspectives. *AIP Advances*, *2*(1), 010701.

- Zhang, X., He, Y., Li, R., Dong, H., & Hu, W. (2016). 2D mica crystal as electret in organic field-effect transistors for multistate memory. *Advanced Materials*, *28*(19), 3755 - 3760. <https://doi.org/10.1002/adma.201506356>
- Zhang, J., Su, C., Rogers, F. J., Darwish, N., Coote, M. L., & Ciampi, S. (2020). Irreproducibility in the triboelectric charging of insulators: Evidence of a non-monotonic charge versus contact time relationship. *Physical Chemistry Chemical Physics*, *22*(20), 11671–11677. <https://doi.org/10.1039/d0cp01317j>
- Zhou, Y. S., Li, S., Niu, S., & Wang, Z. L. (2016). Effect of contact- and sliding-mode electrification on nanoscale charge transfer for energy harvesting. *Nano Research*, *9*(12), 3705–3713.
- Zou, H., Guo, L., Xue, H., Zhang, Y., Shen, X., Liu, X., Wang, Z. L. (2020). Quantifying and understanding the triboelectric series of inorganic non-metallic materials. *Nature Communications*, *11*(1), 1–7. <https://doi.org/10.1038/s41467-020-15926-1>
- Zou, H., Zhang, Y., Guo, L., Wang, P., He, X., Dai, G., Wang, Z. L. (2019). Quantifying the triboelectric series. *Nature Communications*, *10*(1), 1–9. <https://doi.org/10.1038/s41467-019-09461-x>